Novel metallic layered dichalcogenides $Pd_{1-x}M_xTe_2$ (M=Ir, Rh) with $0 \leqslant x \leqslant 1$ in a Fermi liquid scenario

Florencia E. Lurgo [1,*] Raúl E. Carbonio [2] and Rodolfo D. Sánchez[1,†]

[1]*Instituto de Nanociencia y Nanotecnología (INN), CNEA-CONICET, Centro Atómico Bariloche, Comisión Nacional de Energía Atómica and Instituto Balseiro, Universidad Nacional de Cuyo, Av. Bustillo 9500, 8400 San Carlos de Bariloche (RN), Argentina*

[2]*INFIQC (CONICET–UNC), Departamento de Fisicoquímica, Facultad de Ciencias Químicas, Universidad Nacional de Córdoba, Haya de la Torre Esq. Medina Allende, Ciudad Universitaria, X5000HUA Córdoba, Argentina*

The synthesis, structural analysis, and physical properties of dichalcogenide families $Pd_{1-x}Ir_xTe_2$ and $Pd_{1-x}Rh_xTe_2$ with $0 \leqslant x \leqslant 1$ are reported. All compositions show layered structures belonging to the $P\bar{3}m1$ space group at room temperature. These dichalcogenides show $\rho \sim T^2$ regime at low temperatures, indicating a strong electron-electron coupling. At high temperatures, the observed regime is $\rho \sim T$, associated to electron-phonon coupling. These regimes are characteristic of a Fermi liquid behavior. $\rho(T)$ in both families presents two metals with disordered alloys behavior associated with the residual resistivity ratio $\frac{\rho_0}{\rho(300\,K)} \propto x(1-x)$ where x is the Ir or Rh molar fraction. Pauli paramagnetism is observed in all compositions in total agreement with a Fermi liquid behavior with an important effective mass contribution. Hole-type carriers were determined by Seebeck coefficient measurements, and we determined an entropy configuration using the Mott relation for the diffusive regime and an extra term, which is independent of temperature (δ).

I. INTRODUCTION

During past decades, the condensed matter community has extensively studied transition metal dichalcogenides due to their fascinating and diverse physical properties, such as superconductivity, spin-orbit coupling, charge-density wave, topological insulating states, and large magnetoresistance [1–13]. The electronic localization-delocalization transition, in these strongly correlated electron systems, drives to a quantum critical point (QCP). Today, it is well known that superconductivity emerges close to a QCP and the strongly correlated electrons change their behavior from Fermi liquid to a non-Fermi liquid [14,15].

Tellurides with two different metals ($M^*_{1-x}M_xTe_2$) show changes in the spin-orbit Mott states, Debye temperature, and superconductivity compared with the single metal dichalcogenides. Trying to understand these changes, some authors studied different solid solution metal tellurides. Takubo *et al.* studied the compounds $Ir_{1-x}Pt_xTe_2$ with ($0 < x < 0.12$) by using resonant elastic x-ray scattering and resonant inelastic x-ray scattering techniques, and demonstrated that a charge-density wave can coexist with superconductivity [16]. Guo *et al.* synthesized the compounds $Ir_{0.95-x}Rh_xTe_2$ with ($0 \leqslant x \leqslant 0.52$) suggesting that electron-electron/phonon correlation strength is an important factor that increases the temperature of superconductivity (T_c) [17]. Hooda and Yadav determined that $PdTe_2$ and $Cu_{0.04}PdTe_2$ shows a liquid Fermi behavior with two regimes in the electrical resistivity.

These regimes are associated with electron-electron scattering (at low temperature $\rho \sim T^2$) and electron-phonon coupling (higher temperatures $\rho \sim T$). Also, it is observed that by doping $PdTe_2$ with Cu, T_c increases as electron-electron scattering and effective mass [18]. We have previously reported the synthesis and crystallographic analysis of the novel solid solutions $Rh_{1-x}Ir_xTe_2$ with ($0 \leqslant x \leqslant 1$) observed similar results as Hooda *et al.*, given an electrical resistivity and magnetic response as Fermi liquid behavior [19].

These observations prompt a comprehensive exploration of the electrical and thermal transport dispersion mechanism in mixed metal chalcogenides, although the electronic (electrical, thermal) transport properties are lacking in the literature. Therefore, studying these properties opens a novel line of research, with the aim of understanding the electric transport behavior of these compounds and whether Fermi liquid or/and Fermi gas pictures explain it.

In order to explore similar systems, we decided to synthesize two novel families of dichalcogenides, $Pd_{1-x}Ir_xTe_2$ and $Pd_{1-x}Rh_xTe_2$ ($0 \leqslant x \leqslant 1$), and present their crystallographic, electric, and magnetic characterization. The aim of this work is determine whether the Fermi liquid behavior is applicable to these novel families of dichalcogenides.

II. EXPERIMENT

Polycrystalline samples of $Pd_{1-x}Ir_xTe_2$ and $Pd_{1-x}Rh_xTe_2$ with $x = 0, 0.25, 0.50, 0.75$, and 1 were synthesized using a solid-state method with elemental precursors (Pd, Ir, Rh, and Te high purity 99.9% STREM) in vacuum evacuated quartz ampoules. Table I shows the synthesis conditions to obtain the purest version of each sample. Samples of $IrTe_2$ and $RhTe_2$

---

*Corresponding author: florencialurgo@gmail.com
†Corresponding author: rodolfosanchez@cnea.gob.ar

TABLE I. Synthesis conditions for $Pd_{1-x}Ir_xTe_2$ and $Pd_{1-x}Rh_xTe_2$.

Sample	$PdTe_2$	$Pd_{0.75}Ir_{0.25}Te_2$	$Pd_{0.50}Ir_{0.50}Te_2$	$Pd_{0.25}Ir_{0.75}Te_2$	$IrTe_2$
Thermal	500 °C	700 °C	750 °C	800 °C	950 °C 6 h+
Treatment	24 h	24 h	24 h	24 h	600 °C 18 h
Sample	$PdTe_2$	$Pd_{0.75}Rh_{0.25}Te_2$	$Pd_{0.50}Rh_{0.50}Te_2$	$Pd_{0.25}Rh_{0.75}Te_2$	$RhTe_2$
Thermal	500 °C	700 °C	800 °C	925 °C	1100 °C
Treatment	24 h	36 h	48 h	60 h	96 h

were synthesized using the thermal treatment described by Lurgo *et al.* [19]. All compositions were synthesized with a temperature ramp of 5 °C/min in the warming-up process and a fast cooling down (quenching with liquid nitrogen) to obtain the layered phase of interest. The solid solutions were synthesized at temperatures below 1000 °C because the impurity phase PdTe (space group $P6_3/mmc$) is favored at higher temperatures.

The structure was crystallographically characterized using x-ray powder diffraction (XRPD) with a PANalytical X'Pert Pro diffractometer using Bragg-Brentano geometry with a PIXcel detector at room temperature (RT). Crystal structure refinements were performed by using the Rietveld method [20] with the FULLPROF SUITE program [21]. Scanning electronic microscopy (SEM) images were collected in two different microscopes: FE-SEM Sigma and SEM-FEG FEI Nova Nano SEM 230. Energy dispersive x-ray spectroscopy (EDAX) measurements were performed at a SEM-FEG FEI. Magnetization measurements were performed in a commercial MPMS-5S superconducting quantum interference device magnetometer on powdered samples in gelatin capsules from 5 to 300 K at 5000 Oe. Temperature dependence of electrical resistivity [$\rho(T)$] and Seebeck effect [$S(T)$] experiments were performed in a multipurpose equipment with two sample holder lances, respectively. Pellets of the samples were cut into a rectangular polyhedron prism of approximately $11 \times 2 \times 2 \, mm^3$. $\rho(T)$ was measured in the temperature range 5–300 K using a cryostat with liquid helium, while $S(T)$ was measured between 77 and 300 K using a cryostat with liquid nitrogen. To measure the Seebeck effect, two Lake Shore 330 temperature controllers and an HP 34420A nanovoltmeter were used. For electrical resistivity measurements a programmable Keithley 6220 DC current source using a constant electrical current between 0.1 and 100 mA and the same nanovoltmeter and temperature controller were used.

In the Seebeck experiment, we used the same experimental arrangement with copper probes to measure the voltage difference reported for our group in Lurgo *et al.* [19].

III. RESULTS AND DISCUSSION

A. Crystallographic and structural characterization

The XRPD data of $Pd_{1-x}Ir_xTe_2$ and $Pd_{1-x}Rh_xTe_2$ with $x = 0, 0.25, 0.50, 0.75,$ and 1 were collected at RT and correctly refined using space group No. 164, $P\bar{3}m1$ (see Fig. 1 and Figs. S1 and S2 of the Supplemental Material [22]). Tables II and III summarize the refined unit-cell parameters, Te and Pd/Rh/Ir occupancies, and reliability factors. In this layered structure, $Rh^{4+}/Ir^{4+}/Pd^{4+}$ cations are randomly distributed in the $1a$ Wyckoff sites (0,0,0). The data of $IrTe_2$ was obtained

from synchrotron radiation-XRPD measurements at 300 K from Lurgo *et al.* [19]. $IrTe_2$ and $RhTe_2$ samples show impurities of around 1% w/w (weight/weight) of the precursor metals, in total agreement with Lurgo *et al.* [19]. In addition, the composition of $Pd_{0.75}Ir_{0.25}Te_2$ presents 1% w/w of PdTe as an impurity. The rest of the compositions do not show impurities refining the XRPD patterns. Small variations of lattice parameters a, b, and c with composition is observed at RT in agreement with the similar ionic radii of metal cations: r (Pd^{4+}) 0.615, r (Ir^{4+}) 0.625, and r (Rh^{4+}) 0.615 Å. Metal cations (M) are octahedrally coordinated by six Te^{2-} ions, and the face sharing of MTe_6 octahedra forms MTe_2 layers. These

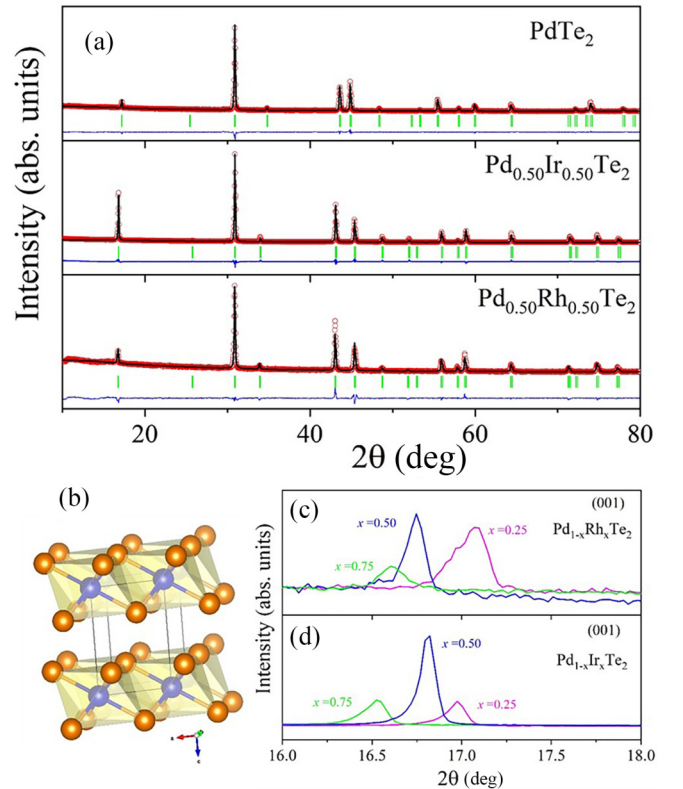FIG. 1. (a) Refined XRPD pattern for compositions $PdTe_2$, $Pd_{0.50}Ir_{0.50}Te_2$, and $Pd_{0.50}Rh_{0.50}Te_2$. Red circles: experimental pattern; black line: calculated pattern; blue line: difference between observed and calculated pattern; green vertical bars: Bragg reflections. (c) $P\bar{3}m1$ structure using the VESTA program [24]. Blue spheres: metal ions ($Rh^{4+}/Ir^{4+}/Pd^{4+}$); orange spheres: Te^{2-} ions. (c),(d) Evolution of the intensity of (001) reflection vs 2θ for compositions with $x = 0.25, 0.50,$ and 0.75 for $Pd_{1-x}Rh_xTe_2$ (c) and $Pd_{1-x}Ir_xTe_2$ (d).

TABLE II. $Pd_{1-x}Ir_xTe_2$ at RT. Refined unit-cell parameters, Te and Pd/Ir occupancies, refined compositions, and reliability factors obtain from XRPD. Note: Nominal compositions are written in the text.

Compound	$PdTe_2$	$Pd_{0.75}Ir_{0.25}Te_2$	$Pd_{0.50}Ir_{0.50}Te_2$	$Pd_{0.25}Ir_{0.75}Te_2$	$IrTe_2$
a (Å)	4.0378(6)	4.0172(1)	3.9930(3)	3.9616(5)	3.9297(2)
b (Å)	4.0378(6)	4.0172(1)	3.9930(3)	3.9616(5)	3.9297(2)
c (Å)	5.1546(9)	5.2250(2)	5.2749(5)	5.3578(8)	5.3989(5)
V (Å^3)	72.781(2)	73.024(4)	72.836(2)	72.820(2)	72.201>(1)
α (deg)	90	90	90	90	90
β (deg)	90	90	90	90	90
γ (deg)	120	120	120	120	120
Pd 1a (0,0,0)					
Occ	0.083(1)	0.051(1)	0.033(2)	0.021(1)	
Ir 1a (0,0,0)					
Occ		0.033(1)	0.050(1)	0.062(1)	0.083(3)
Te 2d (1/3,2/3, z)	0.268(2)	0.742(2)	0.745(4)	0.743(2)	0.748(3)
z	0.164(2)	0.173(2)	0.167(1)	0.167(2)	0.167(2)
Occ					
R_p (%)	17.4	23.8	12.9	18.4	20.7
R_{wp} (%)	4.51	22.1	12.3	15.7	15.1
R_{expt} (%)	1.79	3.96	2.92	3.29	3.92
R_{Bragg} (%)	6.31	7.67	7.11	9.48	3.78
R_{factor} (%)	4.44	5.22	4.68	7.37	3.32
Refined compositions	$PdTe_{1.97}$	$Pd_{0.61}Ir_{0.38}Te_2$	$Pd_{0.40}Ir_{0.60}Te_2$	$Pd_{0.25}Ir_{0.75}Te_2$	$IrTe_2$

layers are bonded by Te-Te bonding rather than weak van der Waals forces [23]. We performed EDAX measurements in three different zones in each sample and determine the composition, in total agreement with Rietveld analysis (see Fig. 2).

B. Magnetic behavior

We subtracted the diamagnetic contribution of the gelatin capsule ($\chi_{capsule} \approx -4.01 \times 10^{-7} \frac{emu}{g}$) and the diamagnetic contribution of each of the atoms in each compound from the magnetic susceptibility (M/H). To subtract

TABLE III. $Pd_{1-x}Rh_xTe_2$ at RT. Refined unit-cell parameters, Te and Pd/Rh occupancies, refined compositions, and reliability factors obtained from XRPD. Note: Nominal compositions are written in the text.

| Compound	$PdTe_2$	$Pd_{0.75}Rh_{0.25}Te_2$	$Pd_{0.50}Rh_{0.50}Te_2$	$Pd_{0.25}Rh_{0.75}Te_2$	$RhTe_2$
a (Å)	4.0378(6)	4.0180(4)	3.9933(2)	3.9571(3)	3.9250(2)
b (Å)	4.0378(6)	4.0180(4)	3.9933(2)	3.9571(3)	3.9250(2)
c (Å)	5.1546(9)	5.1886(5)	5.2884(3)	5.3503(9)	5.4031(4)
V (Å^3)	72.781(2)	72.546(2)	73.032(2)	72.554(1)	72.085(1)
α (deg)	90	90	90	90	90
β (deg)	90	90	90	90	90
γ (deg)	120	120	120	120	120
Pd 1a (0,0,0)					
Occ	0.083(1)	0.062(2)	0.035(2)	0.021(2)	
Rh 1a (0,0,0)					
Occ		0.021(2)	0.049(2)	0.062(2)	0.102(5)
Te 2d (1/3,2/3, z)					
z	0.268(2)	0.744(6)	0.259(6)	0.756(5)	0.746(1)
Occ	0.164(2)	0.152(2)	0.168(2)	0.158(2)	0.167(2)
R_p (%)	17.4	40.1	45.2	71.3	27
R_{wp} (%)	4.51	25.0	29.4	43.9	25.4
R_{expt} (%)	1.79	11.54	8.55	14.64	1.62
R_{Bragg} (%)	6.31	5.52	22.2	14.8	12.9
R_{factor} (%)	4.44	4.63	21.2	11.7	5.88
Refined compositions	$PdTe_{1.97}$	$Pd_{0.75}Rh_{0.25}Te_{1.83}$	$Pd_{0.42}Rh_{0.58}Te_2$	$Pd_{0.25}Rh_{0.75}Te_{0.95}$	$Rh_{1.22}Te_2$
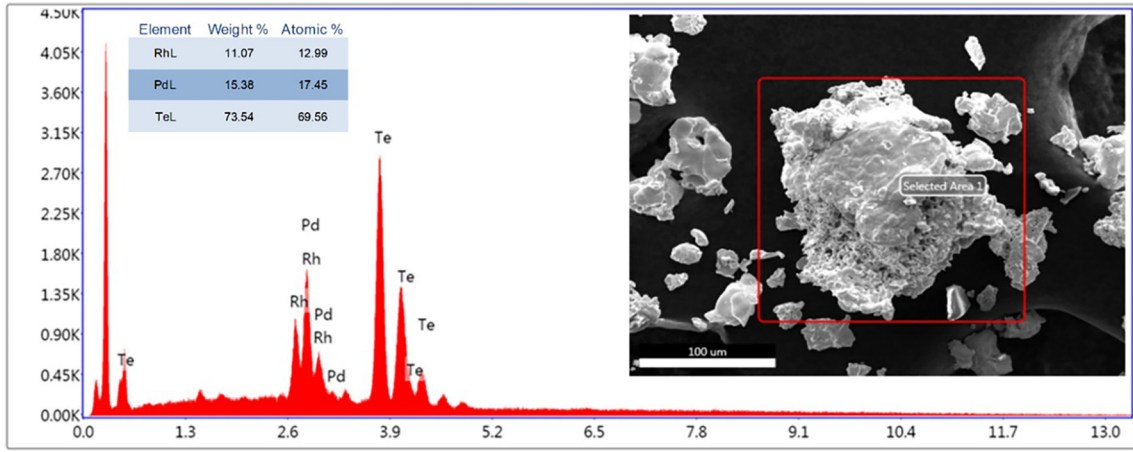
FIG. 2. EDAX analysis of $Pd_{0.50}Rh_{0.50}Te_2$. Inset left: Quantification of the components. Inset right: SEM image of the analyzed zone.

these contributions, we used the corrected Pascal constants χ_{Di} [25]:

Te^{2-}	Rh^{4+}	Ir^{4+}	Pd^{4+}
-70×10^{-6} emu/mol	-18×10^{-6} emu/mol	-29×10^{-6} emu/mol	-18×10^{-6} emu/mol

In Figs. 3(a) and 4(a), we show the thermal evolution of χ for $Pd_{1-x}Ir_xTe_2$ and $Pd_{1-x}Rh_xTe_2$, respectively. At high T, these compounds show that the magnetic susceptibility is temperature independent and correspond to the delocalized conduction electrons. This Pauli paramagnetism behavior is characteristic of metals. Below 100 K, the Curie paramag-
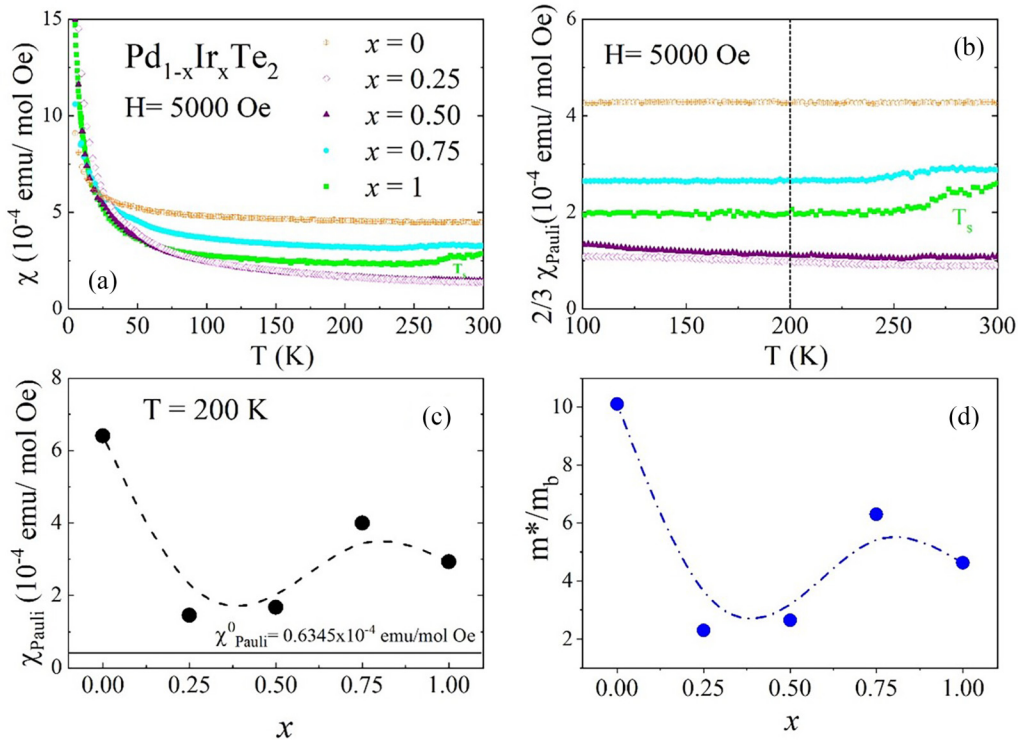

FIG. 3. (a) Magnetic susceptibility vs T for $Pd_{1-x}Ir_xTe_2$ ($0 \leqslant x \leqslant 1$). T_S is the observed phase transition temperature for $IrTe_2$ ($x = 1$). (b) For all the compositions without a Curie tail and in order to better visualize the results, we plotted the susceptibility values as a function of T in the range 100–300 K, which have the Pauli and Landau contributions, equivalent to 2/3 of Pauli susceptibility. (c) In black dots, χ at 200 K vs x, which is compared with estimated $\chi_{Pauli}^0 = 0.6345 \times 10^{-4} \frac{emu}{mol\ Oe}$ (continuous black line). (d) The estimated effective mass ratio (m^*/m_b) vs x (blue dots). Dashed lines show an approximate values variation.
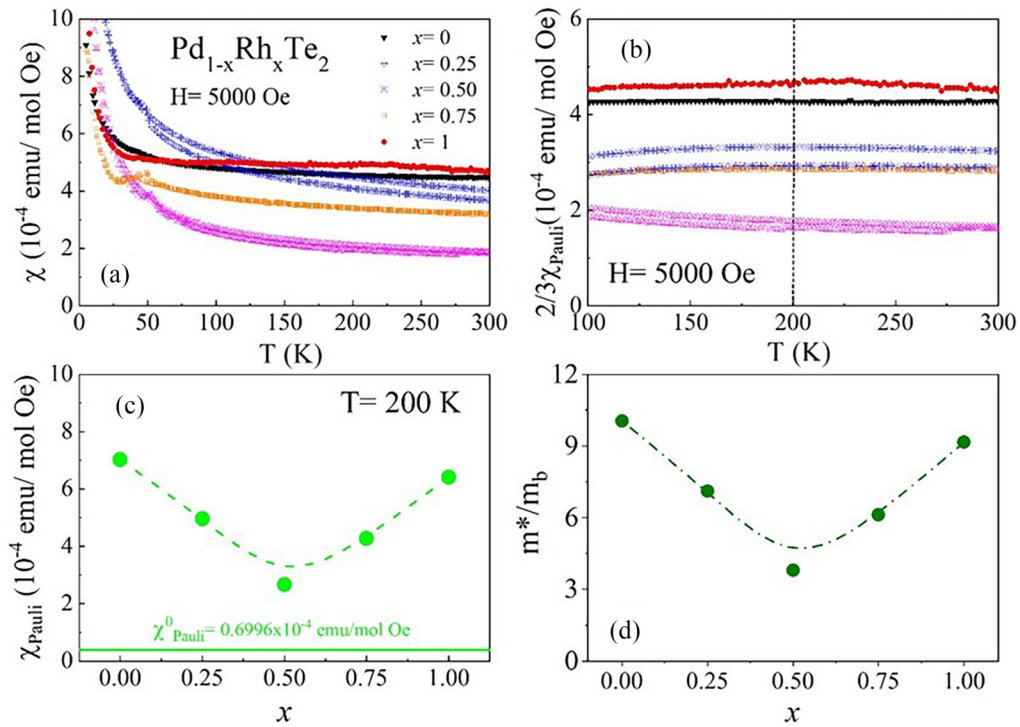
FIG. 4. (a) Magnetic susceptibility vs T for $Pd_{1-x}Rh_xTe_2$ ($0 \leqslant x \leqslant 1$). (b) For all the compositions without a Curie tail and in order to better visualize the results, we plotted the susceptibility values as a function of T in the range 100–300 K, which have the Pauli and Landau contributions, equivalent to 2/3 of Pauli susceptibility. (c) In green dots, χ at 200 K as a function of x, which is compared with estimated $\chi^0_{Pauli} = 0.6996 \times 10^{-4} \frac{emu}{mol\ Oe}$ (continuous green line). (d) The estimated effective mass ratio (m^*/m_b) vs x (olive dots). Dashed lines show an approximative value variation.

netism is observed, which can be associated, for example, to paramagnetic impurities or superparamagnetic clusters [26–28]. These can come from impurities that cannot be detected by conventional XRPD or EDAX techniques. According to the metallic Stoner susceptibility, the corrected $\chi(T)$ data [26,29] are as follows:

$$\chi(T) = \chi_{Pauli} + \chi_{Landau} + \frac{C}{T - \theta} + aT^2,$$

where the third and fourth terms are the Curie paramagnetism of impurities and the high-order temperature-dependent term in the Pauli susceptibility, respectively. The first two terms are the Pauli and Landau paramagnetism. Using this formula, the Curie tail was subtracted [Figs. 3(b) and 4(b)], and only the contribution of the Pauli paramagnetism is observed. These results are observed in similar chalcogenides [29].

We observe in $IrTe_2$ a jump at 280 K (T_s) due to the phase transition in agreement with our previous report [19]. In the plotted warming curve of $\chi(T)$ of $Pd_{0.25}Rh_{0.75}Te_2$, the small peak at around 50 K is a consequence of partial oxygen contamination on the sample [30,31]. After the warming process, the peak was not present in the subsequent run.

Using the Fermi gas model of noninteracting electrons that predicts that Pauli magnetic susceptibility $\chi^0_{Pauli} = \mu_B^2 D(\epsilon_F)$, we could calculate χ^0_{Pauli} for each dichalcogenide family. For $Pd_{1-x}Ir_xTe_2$, we interpolated the values of density of states calculations from literature, between $PdTe_2$ [$D(\epsilon_F) = 1.75$ states/eV] and $IrTe_2$ [$D(\epsilon_F) = 1.94$ states/eV] [32,33],

with these data, and we obtain an average of Pauli susceptibility $\chi^0_{Pauli} = 0.6345 \times 10^{-4} \frac{emu}{mol\ Oe}$. In the other case, using $D(\epsilon_F)$ $PdTe_2 = 1.75$ states/eV and $D(\epsilon_F)$ $RhTe_2 = 2.32$ states/eV [32,34] for the solution $Pd_{1-x}Rh_xTe_2$, we determined an average of $\chi^0_{Pauli} = 0.6996 \times 10^{-4} \frac{emu}{mol\ Oe}$. The val-
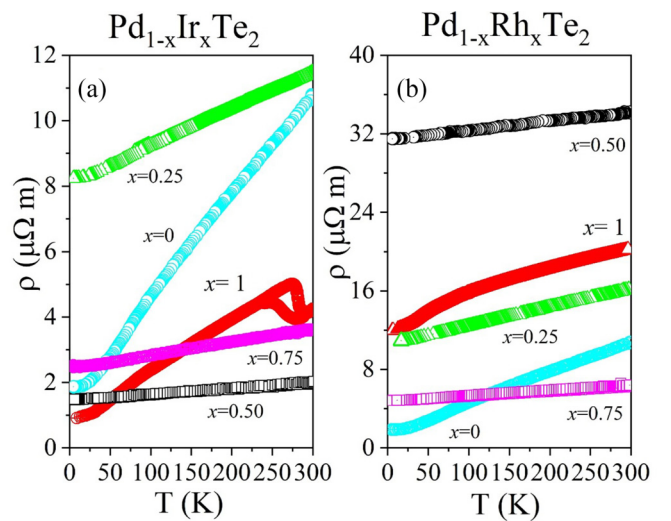
FIG. 5. Electrical resistivity as a function of T for $Pd_{1-x}Ir_xTe_2$ (a) and $Pd_{1-x}Rh_xTe_2$ (b). In $IrTe_2$ is observed hysteresis between the warming and cooling process, which is associated to the first-order structural transition [19].
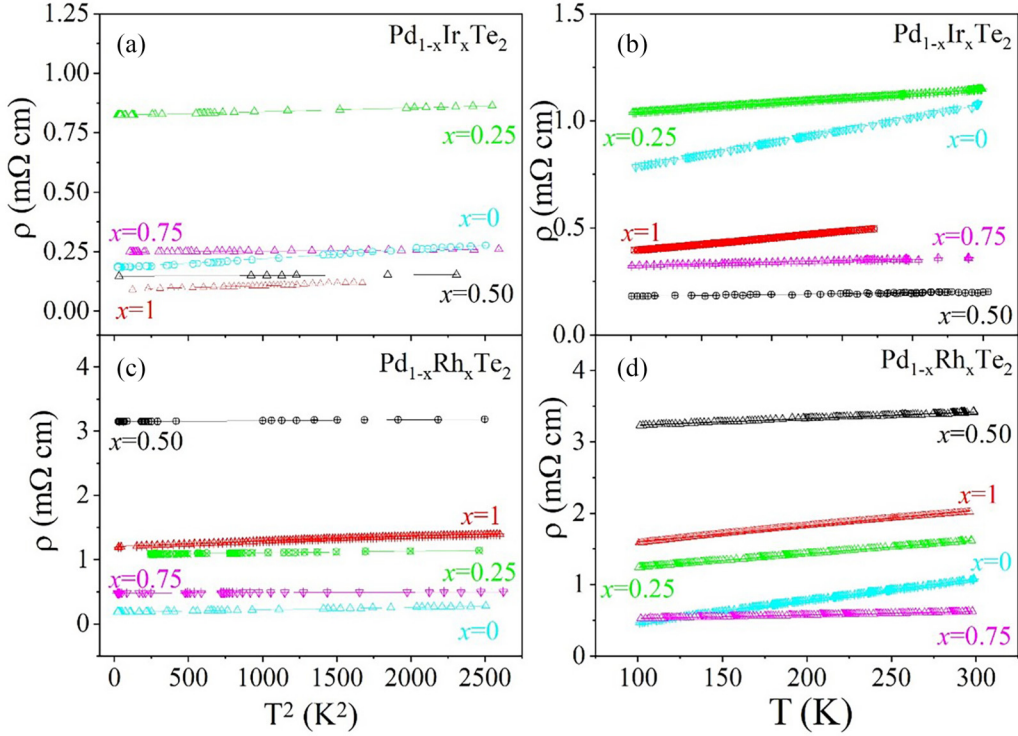
FIG. 6. In dots, the experimental data of electrical resistivity vs temperature and in dashed lines the linear fit for all the compositions. In (a) and (c) the data were fitted using expression $\rho(T^2) = \rho_0 + A_{e-e}T^2$ for $Pd_{1-x}Ir_xTe_2$ and $Pd_{1-x}Rh_xTe_2$, respectively, between 5 and 50 K. In (b) and (d) data were fitted using expression $\rho(T) = \rho^* + A_{e-ph}T$ for $Pd_{1-x}Ir_xTe_2$ and $Pd_{1-x}Rh_xTe_2$, respectively, between 100 and 300 K approximately.

ues of $D(\epsilon_F)$ show a low uptrend $D_{PdTe_2}(\epsilon_F) < D_{IrTe_2}(\epsilon_F) < D_{RhTe_2}(\epsilon_F)$, leading to a slight difference of χ^0_{Pauli} for each dichalcogenide family but this cannot explain the experimental variation of the magnetic susceptibility.

In the temperature range 100–300 K, all the compositions show $\chi_{expt} > \chi^0_{Pauli}$; this indicates that the electrons are interacting with each other. In Fig. 3(c), we compared χ_{expt} for each compound at 200 K as a function of x. This temperature was chosen because we previously studied $Rh_{1-x}Ir_xTe_2$ and the $IrTe_2$ compound presents a structural transition close to room temperature. In order to compare the magnetic susceptibility for all family members with the same crystalline structure, we took the values at 200 K [19]. The expected value for a noninteracting system (χ^0_{Pauli}) as a function of x, is represented by a horizontal dashed line. These magnetic susceptibility values can be explained by changes in the effective mass parameter instead of changes in the density of states at the Fermi level. $Pd_{1-x}Ir_xTe_2$ shows an asymmetric curve with nonsystematic behavior; on the other hand, $Pd_{1-x}Rh_xTe_2$ is a symmetric curve with a minimum at $x = 0.5$. This nonsystematic behavior in solid solutions of dichalcogenides has been observed for several authors [18,19,35].

As $\chi_{expt} > \chi^0_{Pauli}$, the estimated contribution of free electron or Pauli magnetic susceptibility should be corrected by a mass enhancement ratio factor (m^*/m_b), which describes electron correlations in the system, where the effective mass is m^* and m_b is the band mass, to reproduce the experimental values, i.e., $\chi_{expt} = (\frac{m^*}{m_b})\chi^0_{Pauli}$. In order to calculate the effective mass ratio (m^*/m_b), we use the ratio $\frac{\chi_{expt}}{\chi^0_{Pauli}} = (\frac{m^*}{m_b})$. The dependence

with x of (m^*/m_b) and of χ_{expt} vs x, can be seen in Figs. 3 and 4.

As χ_{expt} and (m^*/m_b) are directly proportional, the same trend is observed in the plots. In Figs. 3 and 4 it is observed that $Pd_{0.75}Ir_{0.25}Te_2$, $Pd_{0.50}Ir_{0.50}Te_2$, and $Pd_{0.50}Rh_{0.50}Te_2$ show an estimated low electron correlation compared with the rest of the compositions, which indicates less interactions and a Fermi gas behavior. Different effects such as strong corre-
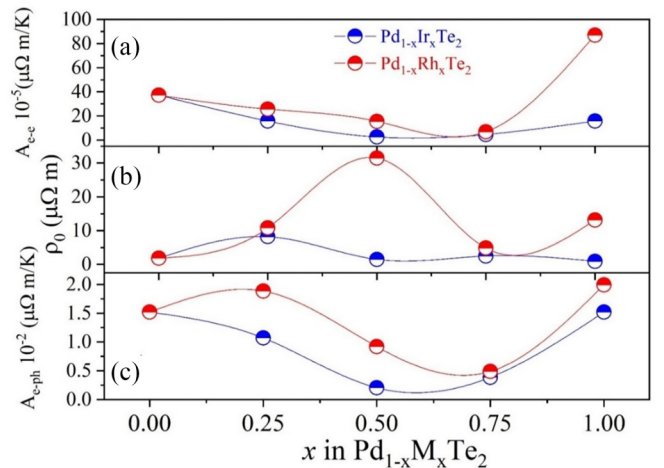

FIG. 7. Residual resistivity (ρ_0), electron-phonon (A_{e-ph}), and electron-electron (A_{e-e}) coefficients as a function of composition for $Pd_{1-x}Ir_xTe_2$ (blue lines) and $Pd_{1-x}Rh_xTe_2$ (red lines).

TABLE IV. Parameters A_{e-e}, ρ_0, and A_{e-ph} for $Pd_{1-x}Ir_xTe_2$ ($0 < x < 1$).

Compound	PdTe$_2$	Pd$_{0.75}$Ir$_{0.25}$Te$_2$	Pd$_{0.50}$Ir$_{0.50}$Te$_2$	Pd$_{0.25}$Ir$_{0.75}$Te$_2$	IrTe$_2$
$A_{e-e}10^{-5}$ ($\mu\Omega\,m/K^2$)	37.2 ± 0.3	15.8 ± 0.1	2.6 ± 0.3	4.7 ± 0.2	15.8 ± 0.2
ρ_0 ($\mu\Omega$ m)	1.839 ± 0.003	8.234 ± 0.001	1.480 ± 0.001	2.485 ± 0.002	0.907 ± 0.008
$A_{e-ph}10^{-2}$ ($\mu\Omega$ m/K)	1.520 ± 0.003	1.070 ± 0.002	0.206 ± 0.009	0.389 ± 0.006	1.520 ± 0.003

lations, site disorder, and proximity to a QCP [36,37] can produce the loss of Fermi liquid characteristics.

C. Electrical and thermal transport properties

1. $\rho(T)$ vs T

In Fig. 5 we show the thermal evolution of electrical resistivity (ρ) for $Pd_{1-x}Ir_xTe_2$ (a) and $Pd_{1-x}Ir_xTe_2$ (b) in a warming and cooling process. IrTe$_2$ shows a hysteresis loop according to the phase transition reported in recent years [19,35]. Temperature dependence of electrical resistivity [$\rho(T)$] can be associated with a Fermi liquid behavior, in total agreement to the magnetic results. At lower temperatures the relation is $\rho(T) \sim T^2$, while at high temperatures is $\rho(T) \sim T$.

At $T < 50$ K the data were fitted using the expression $\rho(T^2) = \rho_0 + A_{e-e} T^2$, where A_{e-e} indicates electron-electron scattering and ρ_0 is the residual electrical resistivity, which is sample dependent [see Figs. 6(a), 6(c), and 7(b)]. The ρ_0 value obtained is in total agreement with the recently estimated residual resistivity for powders and single crystals of PdTe$_2$ and IrTe$_2$ [19,35,38,39].

The A_{e-e} values obtained [see Tables IV and V, and Fig. 7(a)] are similar for other dichalcogenides with strongly correlated electrons, like $Rh_{1-x}Ir_xTe_2$ [19,35], and indicates the important electron-electron scattering in these compounds. As described above, the electron density of states is enhanced by electron-electron scattering; hence, the parameter A_{e-e} has the information of the electron density of states at the Fermi level.

The compounds with two metals are weaker electron-electron scatterers than those with one metal, which can indicate a more Fermi gas behavior than a Fermi liquid, in total agreement with the calculated ($\frac{m^*}{m_b}$) values.

At $T > 50$ K, the data can be fitted with the expression $\rho(T) = \rho^* + A_{e-ph}T$ where A_{e-ph} is the electron-phonon coupling coefficient and ρ^* is the residual resistivity [see Figs. 6(b) and 6(d)]. We obtained the same value of residual resistivity as the $\rho(T) \sim T^2$ relation, which is in agreement with Liu et al. [35]. For simplicity, we use ρ_0 to describe the residual resistivity.

The estimated A_{e-ph} values [see Fig. 7(c)] are large compared with Au and Cu, which indicates a strong electron-phonon coupling in these dichalcogenides. $Pd_{0.75}Rh_{0.25}Te_2$

and RhTe$_2$ present a strong electron-phonon coupling, as observed in similar dichalcogenides, such as $Ir_{0.94-x}Rh_xSe_2$ and $Ir_{0.95-x}Rh_xTe_2$ compounds [17,39].

Assuming metallic alloy behavior, we can represent $\frac{\rho_0}{\rho_T}(x)$ with a parabolic relation (Fig. 8):

for $Pd_{1-x}Ir_xTe_2$,

$$\frac{\rho_0}{\rho_T}(x) = \frac{\rho_{0\ (x=0)}^A}{\rho_{T\ (x=0)}^A}(1-x) + \frac{\rho_{0\ (x=1)}^B}{\rho_{T\ (x=1)}^B}\,x + \xi_{(1)}x(1-x);$$

simplifying,

$$\frac{\rho_0}{\rho_T}(x) = A(1-x) + Bx + \xi_{(1)}x(1-x);$$

and for $Pd_{1-x}Rh_xTe_2$,

$$\frac{\rho_0}{\rho_T}(x) = \frac{\rho_{0\ (x=0)}^A}{\rho_{T\ (x=0)}^A}(1-x) + \frac{\rho_{0\ (x=1)}^C}{\rho_{T\ (x=1)}^C}x + \xi_{(2)}x(1-x);$$

simplifying, $\frac{\rho_0}{\rho_T}(x) = (1-x) + Cx + \xi_{(2)}x(1-x)$,

where A described the relation $\frac{\rho_0}{\rho_T}$ for PdTe$_2$, B for IrTe$_2$, and C for RhTe$_2$. Also, ξ is the disorder factor, entropic contribution. The fitted obtained values are $\xi_{(1)} = 2.230$ and $\xi_{(2)} = 1.800$.

Parabolic behavior is observed for both families, a typical behavior of metallic alloys like that of Cu-Au, Ag-Pd, and Pd-Pt [40]. Normally, in the disordered alloys, the electrical resistivity ratio between low temperature and room temperature resistivity values are proportional to $x(1-x)$. This is due to the basic assumption that the disorder alloy can be considered as an ordered periodic structure whose potential is the average of the components metal potentials (Nordheim model and Mathiessen rule [41]). $\frac{\rho_0}{\rho_T}(x) < 1$ is due to the metallic behavior of all the samples.

2. $S(T)$ vs T

In Figs. 9(a) and 9(c) we show the experimental Seebeck coefficient [$S_{expt}(T)$] as a function of temperature and in Figs. 9(b) and 9(d), we plot the absolute Seebeck coefficient for all compositions in the 80–300 K temperature range, which is obtained adding to $S_{expt}(T)$, the $S_{Cu}(T)$ contribution. All the $S(T)$ values are positive, indicating the presence of hole-type carriers.

TABLE V. A_{e-e}, ρ_0, and A_{e-ph} parameters for $Pd_{1-x}Rh_xTe_2$ ($0 \leqslant x \leqslant 1$).

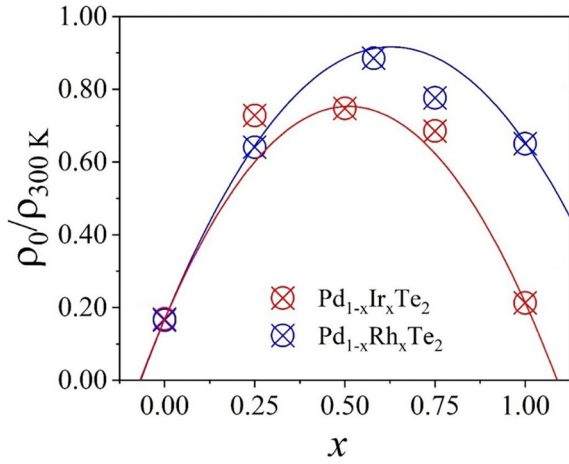| Compound	PdTe$_2$	Pd$_{0.75}$Rh$_{0.25}$Te$_2$	Pd$_{0.50}$Rh$_{0.50}$Te$_2$	Pd$_{0.25}$Rh$_{0.75}$Te$_2$	RhTe$_2$
$A_{e-e}10^{-5}$ ($\mu\Omega\,m/K^2$)	37.2 ± 0.3	25.6 ± 0.5	15.5 ± 0.6	6.9 ± 0.1	86.9 ± 0.3
ρ_0 ($\mu\Omega$m)	1.839 ± 0.003	10.83 ± 0.03	31.49 ± 0.01	4.826 ± 0.01	13.18 ± 0.001
$A_{e-ph}10^{-2}$ ($\mu\Omega$ m/K)	1.520 ± 0.003	1.883 ± 0.002	0.92 ± 0.05	0.49 ± 0.01	1.990 ± 0.004

FIG. 8. $[\frac{\rho_0}{\rho(300\ \mathrm{K})}]$ as a function of refined composition for $Pd_{1-x}Ir_xTe_2$ (red circles) and $Pd_{1-x}Rh_xTe_2$ (blue circles). Continuous lines show the quadratic behavior corresponding to a disorder metallic alloy.

$IrTe_2$ is the only sample that shows a hysteresis in $S(T)$ across the structural phase transition temperature (T_S) [35]. In addition, this sample presents a different behavior than the rest of the compositions studied, showing that the thermopower increases with decreasing temperature. As temperature decreases, the phonon drag phenomenon should be observed, which is proportional to the specific heat [$S_{pd}(T) \sim C_p(T)$]

and its cubic temperature dependence. This phenomenon is present in a wide range of temperatures and a maximum in S should be present, close to $\theta_D/5$, where θ_D is the Debye temperature. $\theta_D \approx 106.2$ K for $PdTe_2$ and $\theta_D \approx 200$ K for $IrTe_2$ as reported in literature [35,42,43]. Taking into account the studies of Liu *et al.* [35], we interpreted that phonon drag contribution in $IrTe_2$ is important and it quickly masks the diffusive contribution. The Seebeck diffusive response is due to the free electrons that generate an electric voltage to equilibrate the gradient of temperature.

This dichalcogenides present a strong metallic behavior, so the Seebeck coefficient is described by

$$S = \frac{\pi^2 k_B^2 T}{3e}\left(\frac{\partial \ln \sigma(E)}{\partial E}\right), \qquad (1)$$

where k_B is the Boltzmann constant, e is the absolute value of electron charge, and $\sigma(E)$ is the distribution of electrical conductivity with energy (E). Experimentally, we observe a linear $S(T)$ behavior at $T > \theta_D/5$, which is expected for compounds with itinerant electrons. However, we have not observed that this linear behavior extrapolates to $S = 0$ at $T = 0$ K in all the compositions as should be expected. Anyway, in order to describe $S(T)$, in the experimental measured temperature range, we propose a phenomenological relation that includes the Mott relation for diffusive regime and an extra term, which
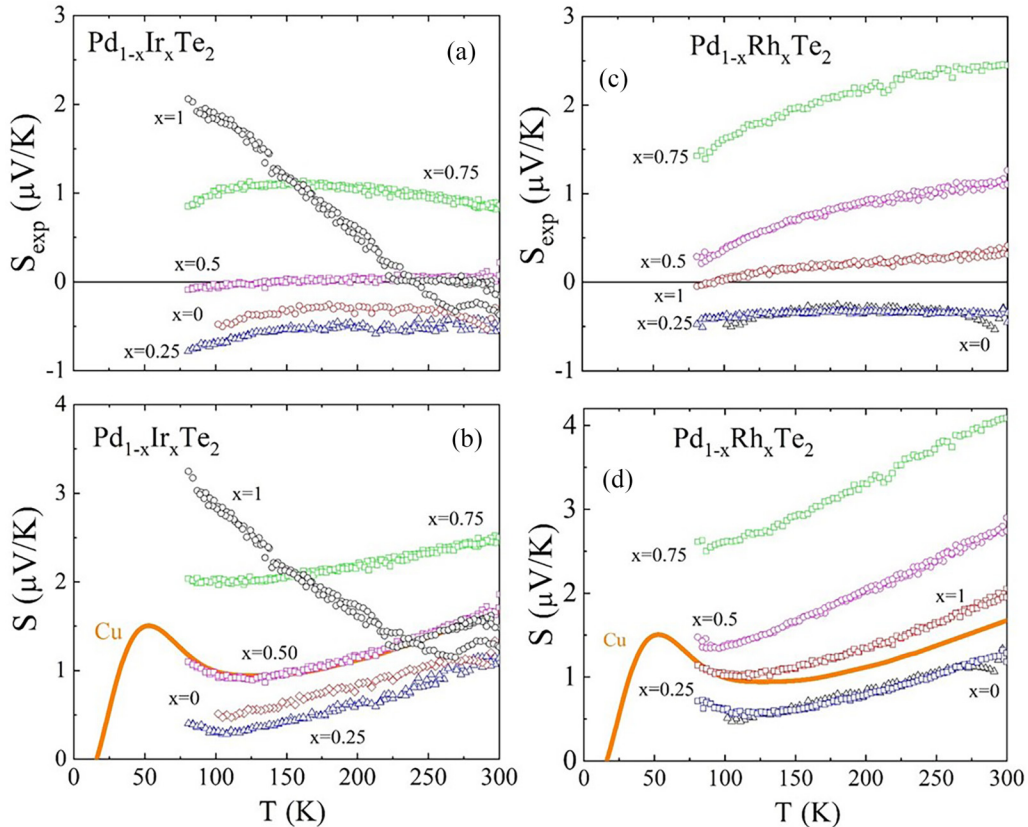
FIG. 9. (a),(c) Experimental Seebeck coefficient for $Pd_{1-x}Ir_xTe_2$ and $Pd_{1-x}Rh_xTe_2$, respectively, including copper (Cu) probe contributions. (b),(d) Absolute Seebeck coefficient of $Pd_{1-x}Ir_xTe_2$ and $Pd_{1-x}Rh_xTe_2$ series, respectively. The copper probe contributions have been subtracted.

TABLE VI. Fitted parameter values obtained using the expression $S_d = \frac{\pi^2 \, k_B^2 \, T}{2e\epsilon_F} + \delta$ for all the dichalcogenides.

Compound	$S_d = \frac{\pi^2 \, k_B^2 \, T}{2e\epsilon_F} + \delta$	
	$10^5 \frac{\pi^2 \, k_B^2}{2 \, e\epsilon_F}$	$\delta \; (\frac{\mu V}{K})$
$PdTe_2$	(389 ± 8)	(0.06 ± 0.01)
$Pd_{0.75}Ir_{0.25}Te_2$	(403 ± 9)	(-0.14 ± 0.02)
$Pd_{0.50}Ir_{0.50}Te_2$	(479 ± 9)	(0.22 ± 0.01)
$Pd_{0.25}Ir_{0.75}Te_2$	(232 ± 9)	(1.74 ± 0.02)
$IrTe_2$	(127 ± 5)	0.0^a
$Pd_{0.75}Rh_{0.25}Te_2$	(442 ± 8)	(-0.08 ± 0.01)
$Pd_{0.50}Rh_{0.50}Te_2$	(674 ± 1)	(0.69 ± 0.02)
$Pd_{0.25}Rh_{0.75}Te_2$	(777 ± 8)	$(1.77\pm\pm0.02)$
$RhTe_2$	(678 ± 8)	(0.14 ± 0.02)

^{a}For $IrTe_2$, δ was obtained from literature [35].

is independent of temperature (δ):

$$S_d = \frac{\pi^2 k_B^2 \, T}{2e\epsilon_F} + \delta, \qquad (2)$$

where ϵ_F is the Fermi energy and δ can be attributed to entropy configurational contributions associated with disorder, or a remanent phonon drag tail.

Table VI and Fig. 10 show the fitted values obtained for the $Pd_{1-x}Ir_xTe_2$ and $Pd_{1-x}Rh_xTe_2$ series using Eq. (2). We did not include the $IrTe_2$ data in Fig. 10, since Liu *et al.* published the thermopower measurements at 5–300 K with a phonon drag contribution at lower T and $S = 0$ at $T = 0$ K [35]. As $Pd_{0.25}Ir_{0.75}Te_2$ and $Pd_{0.25}Rh_{0.75}Te_2$ present a higher δ value, compared with the other compositions, we attribute this to a possible remanent phonon drag behavior or more disorder in these compounds. Each family of dichalcogenides presents similar slope values, except for $Pd_{0.25}Ir_{0.75}Te_2$ and $IrTe_2$. For the first compound, we assume more disorder in agreement with the higher δ value. The reduction of $S(T)$ in

FIG. 10. In dots, Seebeck data, and in dashed lines, the linear fit using the expression $S_d - \delta = \frac{\pi^2 k_B^2 T}{2e\epsilon_F}$ for (a) $Pd_{1-x}Ir_xTe_2$ and (b) $Pd_{1-x}Rh_xTe_2$.

the temperature range 220–260 K, observed in $IrTe_2$, is due to the reconstruction of the Fermi surface across the structural transition [19,35].

Figures 10(a) and 10(b) show the Seebeck fitted data (dashed lines), for all compositions, using the phenomenological expression $S_d - \delta = \frac{\pi^2 k_B^2 \, T}{2e\epsilon_F}$. A diffusive Seebeck behavior is observed and consequently, the thermopower is increased by a disorder factor. The diffusive behavior of $IrTe_2$ is described experimentally in literature [35].

We cannot correlate the Fermi liquid response with the accessible experimental temperature range. The Fermi liquid behavior is clearly observed in electrical resistivity and magnetic susceptibility experiments. To observe the corresponding effective mass presence in the diffusive regime in Seebeck data, we would need to explore a wider experimental temperature range inclusive above 300 K [44].

The phenomenological expression proposed in the Seebeck section follows the Heikes formula, which proposes that the thermopower in metals and semiconductors is governed at high temperatures, by changes in entropy [45]. In the studied dichalcogenides, this behavior may be due to polarons that jump for the vacancies in the M site and generate the strong observed electron-electron correlation. The entropy changes that govern the Seebeck coefficient (δ) in these compounds are in total agreement with the determined disorder metallic alloy behavior. They also explain the scattered values obtained in ρ_0 and justify the nonsystematic behavior in the measurements of $\chi(T)$, $\rho(T)$, and $S(T)$. Each composition exhibits changes in entropy that can be given by orbital or local degeneracy of the electronic configuration on the site without (with) a hole carrier [45], which is very difficult to calculate. The influence of entropy on the electric transport and thermopower of these dichalcogenides is a novelty and complements similar reported works [19,35].

In summary, by adding a second metal in $PdTe_2$, the electron correlation and change in effective mass decrease, leading to greater Fermi gas behavior. In the measured temperature range (5–300 K), the electric resistivity results can be explained as disorder metallic alloys with an important entropic factor dominated the transport mechanism in the compounds with two metals.

IV. CONCLUSIONS

We have synthesized and characterized the structural, magnetic, electric, and thermoelectric properties of $Pd_{1-x}Ir_xTe_2$ and $Pd_{1-x}Rh_xTe_2$ ($0 \leqslant x \leqslant 1$). Fast cooling from synthesis temperature was essential to obtain the metastable layered phase $P\bar{3}m1$ for all compositions.

All the compositions present metallic behavior, dominated by electron-electron correlations, and the expected magnetic Pauli susceptibility is amplified by an effective mass factor. These characteristics correspond to a Fermi liquid behavior. On the other hand, the compositions $x = 0.5$ present lower electron-electron correlations and lose the Fermi liquid character. The electrical resistivity shows for the two different series of compounds the typical disordered metal alloy behavior with a parabolic dependence with the composition.

Seebeck experiments allowed the determination of hole-type carriers for all compositions and a dominating electronic
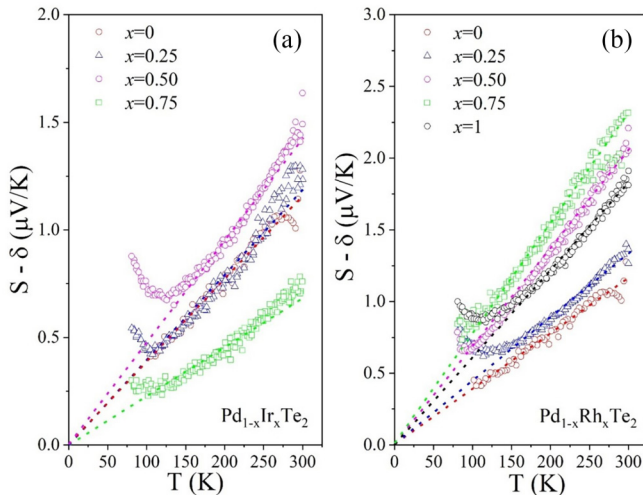
diffusion mechanism. A complete description of the experimental data can be done by a phenomenological formula that includes two terms. One of them is the Mott diffusion contribution with the typical linear temperature dependence, while the second one is a nondependent temperature term. It has nonsystematic behavior with the composition. Nevertheless, this could be due to entropic changes associated with the aleatory amount of cation vacancies present in the samples.

[1] Q. H. Wang, K. Kalantar-Zadeh, A. Kis, J. N. Coleman, and M. S. Strano, Electronics and optoelectronics of two-dimensional transition metal dichalcogenides, Nat. Nanotechnol. **7**, 699 (2012).

[2] R. Lv, J. A. Robinson, R. E. Schaak, D. Sun, Y. Sun, T. E. Mallouk, and M. Terrones, Transition metal dichalcogenides and beyond: Synthesis, properties, and applications of single- and few-layer nanosheets, Acc. Chem. Res. **48**, 56 (2014).

[3] D. Jariwala, V. K. Sangwan, L. J. Lauhon, T. J. Marks, and M. C. Hersam, Emerging device applications for semiconducting two-dimensional transition metal dichalcogenides, ACS Nano **8**, 1102 (2014).

[4] K. F. Mak and J. Shan, Photonics and optoelectronics of 2D semiconductor transition metal dichalcogenides, Nat. Photonics **10**, 216 (2016).

[5] J. Pető, G. Dobrik, G. Kukucska, P. Vancsó, A. A. Koós, J. Koltai, P. Nemes-Incze, C. Hwang, and L. Tapasztó, Moderate strain induced indirect bandgap and conduction electrons in MoS_2 single layers, npj 2D Mater. Appl. **3**, 1 (2019).

[6] S. Subramanian *et al.*, Tuning transport across MoS_2/graphene interfaces via as-grown lateral heterostructures, npj 2D Mater. Appl. **4**, 1 (2020).

[7] E. Morosan, H. W. Zandbergen, B. B. S. Dennis, J. W. G. Bos, Y. Onose, T. Klimczuk, A. P. Ramirez, N. P. Ong, and R. J. Cava, Superconductivity in Cu_xTiSe_2, Nat. Phys. **2**, 544 (2009).

[8] J. A. Wilson and A. D. Yoffe, The transition metal dichalcogenides discussion and interpretation of the observed optical, electrical and structural properties, Adv. Phys. **18**, 193 (1969).

[9] G. Ryu, Superconductivity in Cu-intercalated CdI_2 -type $PdTe_2$, J. Supercond. Novel Magn. **28**, 3275 (2015).

[10] H.-M. Yi, C.-Y. Chen, X. Sun, Z.-J. Xie, Y. Feng, A.-J. Liang, Y.-Y. Peng, S.-L. He, L. Zhao, G.-D. Liu, X.-L. Dong, J. Zhang, C.-T. Chen, Z.-Y. Xu, G.-D. Gu, and X.-J. Zhou, Electronic structure, irreversibility line and magnetoresistance of $Cu_{0.3}Bi_2Se_3$ superconductor, Chin. Phys. Lett. **32**, 067401 (2015).

[11] Y. L. Chen, J. G. Analytis, J. H. Chu, Z. K. Liu, S. K. Mo, X. L. Qi, H. J. Zhang, D. H. Lu, X. Dai, Z. Fang, S. C. Zhang, I. R. Fisher, Z. Hussain, and Z. X. Shen, Experimental realization of a three-dimensional topological insulator, Bi_2Te_3, Science **325**, 178 (2009).

[12] M. N. Ali, J. Xiong, S. Flynn, J. Tao, Q. D. Gibson, L. M. Schoop, T. Liang, N. Haldolaarachchige, M. Hirschberger, N. P. Ong, and R. J. Cava, Large, non-saturating magnetoresistance in WTe_2, Nature (London) **514**, 205 (2014).

[13] D. Ootsuki, S. Pyon, K. Kudo, M. Nohara, M. Horio, T. Yoshida, and A. Fujimori, Electronic structure reconstruction by orbital symmetry breaking in $IrTe_2$, J. Phys. Soc. Jpn. **82**, 093704 (2013).

[14] M. Imada, A. Fujimori, and Y. Tokura, Metal-insulator transitions, Rev. Mod. Phys. **70**, 1039 (1998).

[15] N. Barišić and D. K. Sunko, High-T_c cuprates: A story of two electronic subsystems, J. Supercond. Novel Magn. **35**, 1781 (2022).

[16] K. Takubo, K. Yamamoto, Y. Hirata, H. Wadati, T. Mizokawa, R. Sutarto, F. He, K. Ishii, Y. Yamasaki, H. Nakao, Y. Murakami, G. Matsuo, H. Ishii, M. Kobayashi, K. Kudo, and M. Nohara, Commensurate versus incommensurate charge ordering near the superconducting dome in $Ir_{1-x}Pt_xTe_2$ revealed by resonant x-ray scattering, Phys. Rev. B **97** 205142 (2018).

[17] J. Guo, Y. Qi, and H. Hosono, Structure and superconductivity in pyrite $Ir_{0.95-x}Rh_xTe_2$: A comparison with analogous selenides, Phys. Rev. B **87**, 224504 (2013).

[18] M. K. Hooda and C. Yadav, Electronic transport properties of intermediately coupled superconductors: $PdTe_2$ and $Cu_{0.04}PdTe_2$, Europhys. Lett. **121**, 17001 (2018).

[19] F. E. Lurgo, F. Pomiro, R. E. Carbonio, and R. D. Sánchez, Synthesis and structural, magnetic, electric, and thermoelectric characterization of layered $Rh_{1-x}Ir_xTe_2$ ($0 \leqslant x \leqslant 1$), Phys. Rev. B **105**, 104104 (2022).

[20] H. M. Rietveld, A profile refinement method for nuclear and magnetic structures, J. Appl. Crystallogr. **2**, 65 (1969).

[21] J. Rodriguez-Carvajal, Recent advances in magnetic structure determination by neutron powder diffraction, Phys. B (Amsterdam, Neth.) **192**, 55 (1993).

[22] See Supplemental Material at http://link.aps.org/supplemental/10.1103/PhysRevB.109.094104 for the XRPD patterns for all the compositions.

[23] N. V. Podberezskaya, S. A. Magarill, N. V. Pervukhina, and S. V. Borisov, Crystal chemistry of dichalcogenides MX_2, J. Struct. Chem. **42**, 654 (2001).

[24] K. Momma and F. Izumi, VESTA 3 for three-dimensional visualization of crystal, volumetric and morphology data, J. Appl. Crystallogr. **44**, 1272 (2011).

[25] G. Bain and J. Berry, Diamagnetic corrections and Pascal's constants, J. Chem. Educ. **85**, 4 (2008).

[26] R. D. Sanchez, M. Causa, B. Teresa, A. Seoane, J. Rivas, F. Rivadulla, M. A. López Quintela, J. J. Pérez Cacho, J. Blasco, and J. García, Metal-insulator transition and magnetic proper-

ties of La$_{1-x}$Eu$_x$NiO$_3$ ($0 \leqslant x \leqslant 1$), J. Solid State Chem. **151**, 1 (2000).

[27] R. D. Sanchez, J. Rivas, F. Garcia-Sanz, and M. T. Causa, Approximation to the metal-insulator transition by Gd^{3+} doping in Pauli LaNiO$_3$ perovskite, J. Alloys Compd. **239**, 31 (1996).

[28] R. Roldán, J. A. Silva-Guillén, M. Pilar Lopez-Sancho, F. Guinea, E. Cappelluti, and P. Ordejon, Electronic properties of single-layer and multilayer transition metal dichalcogenides MX_2 (M=Mo, W and X=S, Se), Ann. Phys. (Berlin) **526**, 347 (2014).

[29] S. Kikuchi, M. Wakeshima, and Y. Hinatsu, Electrical properties of ternary metal-rich telluride Pd$_2$NiTe$_2$, J. Ceram. Soc. Jpn. **117**, 27 (2009).

[30] Oxygen contamination, MPMS Application Note 1014-210 (Quantum Design, 1997), http:/www.cmag.si/QD-OxygenContamination.pdf

[31] S. Gregory, Magnetic susceptibility of oxygen adsorbed on graphite, Phys. Rev. Lett. **40**, 723 (1978).

[32] O. J. Clark, M. J. Neat, K. Okawa, L. Bawden, I. Marković, F. Mazzola, J. Feng, V. Sunko, J. M. Riley, W. Meevasana, J. Fujii, I. Vobornik, T. K. Kim, T. Hoesch, T. Sasagawa, P. Wah, M. S. Bahramy, and P. D. C. King, Fermiology and superconductivity of topological surface states in PdTe$_2$, Phys. Rev. Lett. **120**, 156401 (2018).

[33] A. F. Fang, G. Xu, T. Dong, P. Zheng, and N. L. Wang, Structural phase transition in IrTe$_2$: A combined study of optical spectroscopy and band structure calculations, Sci. Rep. **3**, 1153 (2013).

[34] C.-S. Lee and G. J. Miller, Vacancy ordering and bonding competition in the group 9 tellurides M$_x$Te$_2$ (M=Rh, Ir; $0.75 \leqslant x \leqslant 2$): A theoretical study, Inorg. Chem. **38**, 5139 (1999).

[35] Y. Liu, H. Lei, K. Wang, M. Abeykoon, J. B. Warren, E. Bozin, and C. Petrovic, Thermoelectric studies of Ir$_{1-x}$Rh$_x$Te$_2$ ($0 < x < 0.3$), Phys. Rev. B **98**, 094519 (2018).

[36] H. v. Löhneysen, A. Rosch, M. Vojta, and P. Wölfle, Fermi-liquid instabilities at magnetic quantum phase transitions, Rev. Mod. Phys. **79**, 1015 (2007).

[37] E. Svanidze, L. Liu, B. Frandsen, B. D. White, T. Besara, T. Goko, T. Medina, T. J. S. Munsie, G. M. Luke, D. Zheng, C. Q. Jin, T. Siegrist, M. B. Maple, Y. J. Uemura, and E. Morosan, Non-Fermi liquid behavior close to a quantum critical point in a ferromagnetic state without local moments, Phys. Rev. X **5**, 011026 (2015).

[38] G. Cao, W. Xie, W. A. Phelan, J. F. DiTusa, and R. Jin, Electrical anisotropy and coexistence of structural transitions and superconductivity in IrTe$_2$, Phys. Rev. B **95**, 035148 (2017).

[39] J. Guo, Y. Qi, S. Matsuishi, and H. Hosono, T_c maximum in solid solution of pyrite IrSe$_2$-RhSe$_2$ induced by destabilization of anion dimers, J. Am. Chem. Soc. **134**, 20001 (2012).

[40] W. L. McMillan, Transition temperature of strong-coupled superconductors, Phys. Rev. **167**, 331 (1968).

[41] J. S. Dugdale, *The Electrical Properties of Metals and Alloys* (Dover Publications, New York, 2016).

[42] A. Vasdev, A. Sirohi, M. K. Hooda, C. S. Yadav, and G. Sheet, Enhanced, homogeneously type-II superconductivity in Cu-intercalated PdTe$_2$, J. Phys.: Condens. Matter **32**, 125701 (2020).

[43] G. Anemone *et al.*, Electron–phonon coupling in superconducting 1T-PdTe$_2$, npj 2D Mater. Appl. **5**, 25 (2021).

[44] S. Kremer and R. Frésard, Thermoelectric transport properties of an apparent Fermi liquid: Relation to an analytic anomaly in the density of states and application to hole-doped delafossites, Ann. Phys. **524**, 21 (2012).

[45] P. Chaikin and G. Beni, Thermopower in the correlated hopping regime, Phys. Rev. B **13**, 647 (1976).